



Numerical Investigation of Jet-Wake Interaction for a Dual-Bell Nozzle

Simon Loosen¹  · Matthias Meinke¹ · Wolfgang Schröder¹

Received: 27 March 2019 / Accepted: 29 July 2019 / Published online: 3 September 2019
© Springer Nature B.V. 2019

Abstract

The turbulent wake of a planar generic space launcher equipped with a dual-bell nozzle is numerically investigated to examine the interaction of the dual-bell nozzle jet and the wake flow. The simulation is performed at transonic freestream condition, i.e., freestream Mach number $Ma_\infty = 0.8$ and freestream Reynolds number based on the launcher thickness $Re_D = 4.3 \cdot 10^5$, with the dual-bell nozzle operating at sea-level mode. A zonal RANS/LES approach is used and the time-resolved flow field data is analyzed by classical spectral analysis and modal decomposition techniques, i.e., proper orthogonal decomposition (POD) and dynamic mode decomposition (DMD). The overall flow topology of the recirculation region downstream of the base and the pressure loads on the outer nozzle fairing are only slightly affected by the modified nozzle shape. However, the changed nozzle flow topology characterized by the flow separation at the nozzle contour inflection leads to a backflow region and an entrainment of the outer flow into the nozzle extension which results in increased pressure loads on the inner nozzle wall. Using spectral, POD, and DMD analyses, the outer wake flow is investigated, revealing a growing and contracting of the separation bubble and an undulating motion of the shear layer similar to the “cross-pumping” and “cross-flapping” motion detected in previous investigations of a configuration with a classical nozzle and a jetless backward facing step setup. The spectral and modal analysis of the nozzle flow shows that the increased pressure loads detected at the inner wall of the nozzle extension are caused by an interaction of the separated shear layer inside the nozzle extension with the shock pattern that leads to a streamwise oscillation of the shock and a pumping or wave-like motion of the shear layer.

Keywords Zonal RANS/LES · Dual-bell nozzle · Proper orthogonal decomposition · Dynamic mode decomposition · Space launcher wake · Backward-facing step

✉ Simon Loosen
s.loosen@aia.rwth-aachen.de

¹ Institute of Aerodynamics and Chair of Fluid Mechanics, RWTH Aachen University, Wüllnerstraße 5a, 52062 Aachen, Germany

1 Introduction

The main stage engine of a classical parallel staging space launcher like the European Ariane 5 operates in a broad altitude range, i.e., from sea-level up to almost vacuum conditions. To prevent flow separation at sea-level mode which would lead to strong side loads, the maximum area ratio of the nozzle is limited. Since the ambient pressure decreases with increasing altitude, a larger area ratio without flow separation would be possible at altitude mode leading to a higher specific impulse and thus, to an increased payload mass. An advanced propulsion concept which avoids this constraint is altitude adaptive nozzles like the dual-bell nozzle with a larger feasible area ratio at altitude conditions. The dual-bell nozzle consists of a conventional bell nozzle, i.e., the base nozzle, and an extension nozzle. The combination of both nozzles results in an abrupt contour inflection. Depending on the nozzle pressure ratio (NPR), which is the ratio of the chamber pressure to the ambient pressure, the dual-bell nozzle features two operating conditions which are shown in Fig. 1. At sea-level mode when NPR is smaller than the transition nozzle pressure ratio (NPR_{tr}), the flow is attached in the base nozzle and a controlled and symmetric flow separation takes place at the abrupt inflection preventing any side loads. At a certain flight altitude, when NPR is greater than NPR_{tr} , the separation point shifts from the inflection to the nozzle exit leading to a symmetric attached flow in the complete nozzle. Due to the larger feasible area ratio, the expansion of the nozzle flow is increased leading to an improved performance at altitude mode compared to classical rocket engines. The dual-bell flow behavior, e.g., the transition behavior, the arising side loads, and the payload gain, has experimentally, e.g., by Stark et al. [1] and Proshchanka et al. [2], and numerically, e.g., by Martelli et al. [3] and Schneider & Genin [4], been investigated proving the functionality of the adaptive nozzle concept. However, the aerodynamic integration of the dual-bell nozzle into the launcher's architecture and the influence of the outer flow onto the dual-bell nozzle flow and its transition behavior have not been investigated, yet.

The outer wake flow is characterized by the separation of the incoming boundary layer at the base shoulder and its subsequent reattachment on the nozzle leading to the formation of a highly dynamic recirculation region. The turbulent wake flow behind the base exhibits many similarities with the flow past a planar backward-facing step (BFS) extensively studied experimentally, e.g., by Bradshaw & Wong [5], Eaton & Johnston [6], Driver et al. [7], and numerically, e.g., by Friedrich & Arnal [8], Silveira Neto et al. [9], Le et al. [10], and Lee & Sung [11]. In all these investigations a variation of the instantaneous impingement location of the separated shear layer by about two step heights around the mean reattachment position is reported. In addition, two basic modes of characteristic frequencies were detected in nearly all of these studies. The low frequency mode at a Strouhal number of

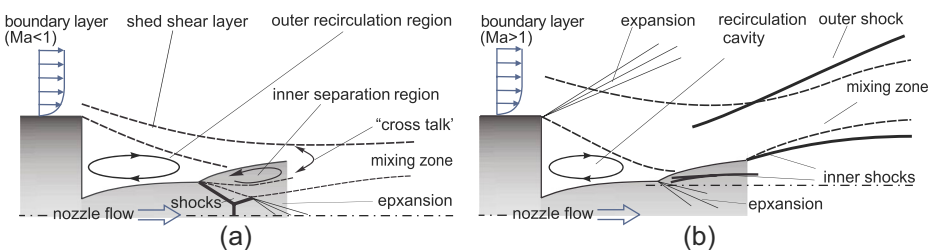


Fig. 1 Schematic of the interaction of the wake flow with a dual-bell nozzle operating at sea-level mode (a) and altitude mode (b)

$Sr_h = 0.012 - 0.014$ based on the step height and the freestream velocity reflects an overall increase and decrease of the separation bubble or shear-layer “flapping” as it is commonly called in the literature. The aforementioned time-dependent variation of the instantaneous reattachment position can be attributed to this “flapping” motion. The higher frequency mode at $Sr_h = 0.065 - 0.08$ is attributed to a Kelvin-Helmholtz like vortex-shedding instability. The studies on planar BFS flows are mainly limited to two-dimensional observations or spanwise averaged flow properties. More recently, Statnikov et al. [12], Scharnowski et al. [13] and Bolgar et al. [14] analyzed the three-dimensional wake of a generic planar launcher consisting of a BFS with a long forebody. It was shown that the reattachment position varies over time not only in the streamwise but also in the spanwise direction leading to a formation of wedge-shaped reattachment regions. Using a dynamic mode decomposition (DMD) analysis, this variation in the reattachment process can be traced back to a coherent longitudinal cross-pumping motion of the recirculation bubble at $Sr_D = 0.04$ ($Sr_h = 0.012$) and a cross-flapping motion of the shear layer at $Sr_D = 0.23$ ($Sr_h = 0.07$), where D is the “thickness” of the launcher.

Besides the presented studies on planar configurations, many experimental and numerical investigations on a large range of different axisymmetric more realistic space launcher configurations ranging from axisymmetric backward-facing steps up to scaled real launchers have been conducted, e.g. Deprés et al. [15], Deck & Thorigny [16], Schrijer et al. [17], and Statnikov et al. [18, 19]. Schrijer et al. used POD to analyze a time series of snapshots of 2D-PIV measurements and detected two dominant wake modes containing the majority of the turbulent kinetic energy. The first low frequency mode captures an oscillating growing and shrinking of the separation zone, most probably being related to the shear-layer “flapping” detected in the planar BFS flows or to the more recently observed three-dimensional cross-pumping motion by Statnikov et al. [12] in a planar space launcher configuration. The second higher frequency mode describes an undulating motion of the shear layer coinciding with the vortex-shedding of the BFS flow (Le et al. [10]) and the cross-flapping motion of the planar space launcher (Statnikov et al. [12]). Statnikov et al. [12] performed a dynamic mode decomposition of the flow around a generic Ariane 5-like configuration to analyze the coherent structures being responsible for side forces occurring for axisymmetric configurations. Three distinct modes at $Sr_D \approx 0.1; 0.2; 0.35$ which could generate buffet were detected. The low frequency mode describes a longitudinal cross-pumping motion of the separation region, the second mode is associated with a cross-flapping motion of the shear layer caused by antisymmetric vortex shedding, and the high frequency mode represents a swinging motion of the shear layer.

In the present study, a planar generic space launcher equipped with a dual-bell nozzle will be investigated at transonic flow conditions to determine the influence of the altitude adaptive nozzle onto the intricate wake-nozzle flow interaction. The analysis will be performed for the dual-bell nozzle operating at sea-level mode i.e., with the inner separation at the contour inflection. In the present study, the flow field of a planar space launcher-like configuration is computed to enable a straightforward validation of the numerical zonal RANS/LES results with experimental pressure values and PIV measurements in the center cross-section [20]. Note that due to the planar geometry a direct transfer of the numerical findings to more realistic axisymmetric launchers is not feasible since the characteristic frequencies and azimuthal wave lengths of the wake modes may differ. However, previous investigations indicated that the dominant wake modes of a planar BFS configuration [12] are comparable with the energetically most dominant wake modes, i.e., a growing and shrinking of the recirculation bubble and an undulating motion of the shear layer of an axisymmetric configuration [17]. Despite the mentioned similarities to axisymmetric wakes,

the study of the present planar configuration, which gives a first impression of the influence of the dual-bell nozzle onto the wake flow, will be complemented by investigations of more realistic axisymmetric free flight configurations to analyze the similarities and differences between planar and axisymmetric wake modes.

Besides classical statistical analyses such as mean and root-mean-square distributions and spectral analyses, POD and DMD are used to analyze the wake and nozzle flow. The most energetic modes are extracted by POD and dynamically highly relevant but low-energy modes are determined by DMD. The investigated flow field is characterized by a superposition of flow structures exhibiting various time and length scales. Therefore, it is challenging to identify the flow mechanisms which are responsible for the dynamic loads acting onto the outer and inner nozzle wall. The POD and DMD methods, which belong to a class of data-driven modal decomposition techniques, enable to isolate spatial modes such that insight into the underlying flow mechanisms is obtained.

The paper is organized as follows. In Section 2, the investigated geometry and the flow parameters are presented. The zonal RANS/LES method, the computational grids, and the POD and DMD algorithms are briefly described. In Section 3, the results of the performed simulations are discussed. First, the wake flow topology including the jet is described and compared to a configuration with a classical thrust optimized parabolic (TOP) nozzle. Then, the pressure loads on the outer and inner nozzle wall are investigated by spectral analysis followed by a modal analysis of the BFS wake and of the flow inside the nozzle by POD and DMD. Finally, conclusions are drawn in Section 4.

2 Computational Approach

In this section, the geometry and flow parameters, the zonal RANS/LES method, the computational grids, and the POD and DMD algorithms are discussed.

2.1 Geometry and flow conditions

The aerodynamic integration of the dual-bell nozzle into the space launcher and the influence of the altitude adaptive nozzle onto the intricate wake-nozzle flow interaction is investigated for a planar generic space launcher-like configuration shown in Fig. 2. The setup is based on the geometry in [21], where a classic TOP nozzle was considered. The launcher model is composed of a main body with a reference thickness of D and a length

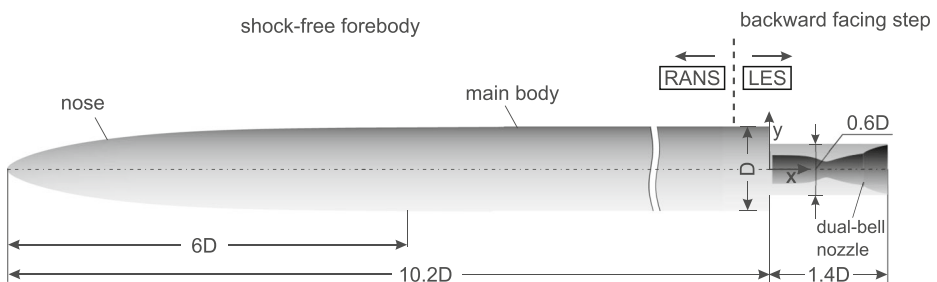


Fig. 2 Geometry parameters of the investigated generic planar transonic configuration

of $4.2D$ and a long shock-free nose with a length of $6D$ to avoid an undesired shock-boundary interaction upstream of the investigated wake flow. The spanwise extent of the planar launcher is $1.2D$. The tail of the launcher including the engine is modeled by a nozzle fairing with a length of $1.4D$ and a thickness of $0.6D$ which is mounted downstream of the main body. The length of the fairing is defined such that an impingement of the shed shear layer shortly upstream of the end of the nozzle occurs which is the most critical condition since the pressure loads are largest around the impingement position. For the inner shape of the nozzle, a dual-bell geometry with a truncated ideal contour (TIC) for the base nozzle and a constant pressure nozzle extension with a design exit Mach number at altitude mode of $Ma_e = 3.3$ is used. The design transition nozzle pressure ratio of the dual-bell nozzle estimated by the method of characteristics combined with an empirical separation law is $NPR_{tr} = 17.2$. For the dual-bell nozzle design and the subsequent simulation, air with a heat capacity ratio of $\gamma = 1.4$ is used. The total pressure of the nozzle is 6 bar and the nozzle pressure ratio is $NPR = 7.62$. The throat height of the nozzle is $0.104D$, the base nozzle exit height is $0.31D$, and the extension nozzle height is $0.56D$ resulting in a total expansion ratio of $\epsilon = 5.38$ and a base nozzle expansion ratio of $\epsilon_{base} = 2.98$. Note that compared to the setup used in Loosen et al. [21] which serves as a reference case for the present investigation, the thickness of the nozzle extension is increased by $0.2D$ due to the particular characteristics of the dual-bell nozzle and the length of the nozzle extension is reduced by $0.6D$ to ensure an impingement of the shed shear layer close to the end of the nozzle. The main body thickness D is chosen as a reference value and the origin of the frame of reference is located at the center of the main body's tail. The x-axis defines the streamwise direction, the z-axis the spanwise direction, and the y-axis is perpendicular to x and z.

Since the dynamic loads feature the highest nominal amplitudes during the transonic stage of the flight trajectory [22], the simulation is performed at a freestream Mach number of $Ma_\infty = 0.8$. An adiabatic no-slip boundary condition is applied at the surface of the planar launcher. The freestream and nozzle flow conditions are summarized in Table 1. They are based on a number of experimental investigations recently performed on the same planar launcher at the Bundeswehr University Munich within the framework of the German Collaborative Research Center Transregio 40 [20]. Note that the static pressure of the freestream and consequently, the nozzle pressure ratio is slightly different to the experimental investigations to guarantee the comparability to the reference configuration with the TOP nozzle.

2.2 Zonal RANS/LES flow solver

The time-resolved computations are performed using a zonal RANS/LES solver which is based on a finite-volume method. The computational domain is split into several zones, see Fig. 3. In the zones where the flow is attached, i.e., the flow around the forebody and inside the base nozzle, the RANS equations are solved. The wake flow characterized by the separated shear layer is determined by an LES.

Table 1 Freestream and nozzle flow conditions

	M	Re_D	U [m/s]	p_0 [Pa]	p [Pa]	NPR	T_0 [K]	T [K]
Freestream (∞)	0.8	$0.43 \cdot 10^6$	257	$1.2 \cdot 10^5$	$0.787 \cdot 10^5$		290	257
Nozzle exit	3.25		628.8	$6 \cdot 10^5$	$0.113 \cdot 10^5$	7.62	290	93.24

The Navier-Stokes equations of a three-dimensional unsteady compressible fluid are discretized second-order accurate using a mixed centered/upwind advective upstream splitting method (AUSM) scheme for the Euler terms. The non-Euler terms are approximated by a second-order accurate centered scheme. For the temporal integration an explicit 5-stage Runge-Kutta method of second-order accuracy is used. The monotone integrated LES (MILES) method determines the impact of the sub-grid scales. The solution of the RANS equations is based on the same discretization method. To close the time-averaged equations the one-equation turbulence model of Fares & Schröder [23] is used. In the simulation, air with a heat capacity ratio of $\gamma = 1.4$ and a Prandtl number of $Pr = 0.72$ is used. For the non-dimensionalized dynamic viscosity and thermal conductivity, an empirical power law, i.e., $\mu = T^{0.72}$ and $\lambda = T^{0.72}$, is used. For a comprehensive description of the flow solver see Statnikov et al. [12, 24].

The transition from the RANS to the LES domain is determined by the reformulated synthetic turbulence generation (RSTG) method developed by Roidl et al. [25, 26], which allows to reconstruct the turbulent fluctuations in the LES inlet plane based on the upstream RANS solution. This method generates turbulent fluctuations as a superposition of coherent structures and extends the idea of the synthetic eddy method (SEM) by Jarrin et al. [27]. The turbulent structures are generated at the inlet plane by superimposing virtual eddy cores, which are defined at random positions \mathbf{x}_i in a virtual volume V_{virt} . This volume encloses the inlet plane and exhibits the dimension of the turbulent length scale l_x , the boundary-layer thickness at the inlet δ_0 , and the width of the computational domain L_z in the streamwise, the wall-normal, and the spanwise direction. To take the inhomogeneity of the turbulent scales in the wall-normal direction into account, the virtual eddy cores are described by different shape factors and length and time scales depending on the wall-normal distance. Having N synthetic eddies, the normalized stochastic velocity fluctuations u'_m at the LES inlet plane are determined by the sum of the contribution $u'^i_m(\mathbf{x}, t)$ of each eddy core i

$$u'_m(\mathbf{x}, t) = \frac{1}{\sqrt{N}} \sum_{i=1}^N \underbrace{\epsilon_i f_{\sigma,m}^i(\mathbf{x} - \mathbf{x}_i)}_{u'^i_m(\mathbf{x}, t)}, \quad (1)$$

where ϵ_i is a random number within the interval $[-1, 1]$, $f_{\sigma,m}^i$ is the shape function of the respective eddy, and the subscript m denotes the Cartesian coordinates in the streamwise, the wall-normal, and the spanwise direction. The final velocity components at the LES inflow plane u_m are composed of an averaged velocity component $u_{RANS,m}$ from the RANS solution and the normalized velocity fluctuations u'_m which are subjected to a Cholesky decomposition A_{mn} to assign the values of the target Reynolds-stress tensor $R_{mn} = A_{mn}^T A_{mn}$ corresponding to the turbulent eddy viscosity of the upstream RANS

$$u_m(\mathbf{x}, t) = u_{RANS,m} + A_{mn} u'^i_m(\mathbf{x}, t). \quad (2)$$

To enable an upstream information exchange, i.e., a full bidirectional coupling of the LES and RANS zones, the time-averaged static pressure of the LES zone is imposed after a transition of three boundary-layer thicknesses at the end of the overlapping zone onto the RANS outflow boundary. The temporal window width used to compute the pressure for the RANS outflow plane is chosen such that high frequency oscillations of the LES pressure field are filtered out. A more detailed description of the zonal RANS/LES method specifying the shape functions and length scales is given in Roidl et al. [25, 26].

2.3 Computational mesh

In the zonal approach, the computational domain is divided into a RANS part enclosing the attached flow around the forebody and inside the base nozzle and an LES grid for the wake shown in Fig. 3. To reduce the computational costs, the simulation is only performed for the upper half of the flow field, i.e., a symmetry condition is imposed in the $y/D = 0$ plane. Note that the symmetry condition imposes a substantial constraint on the turbulent structures in the center plane, i.e., at $y/D = 0$. However, the turbulent eddies are limited to the boundary layer in the nozzle and separated shear layer downstream of the contour inflection and thus, the boundary condition mainly imposes a symmetry onto the shock pattern. The pressure loads on the outer nozzle fairing and the responsible POD and DMD modes detected in the outer wake flow are most likely not affected by the boundary conditions since similar dynamics have been found in previous pure BFS flow configurations. The RANS domain around the forebody extends to approximately $10D$ in the wall-normal direction and ends at $x/D = -0.05$ just upstream of the trailing edge of the main body located at $x/D = 0$. The LES section extends in the streamwise direction from $x/D = -0.5$ to $x/D = 10$ and in the wall-normal direction, like the RANS mesh from $y/D = 0$ to $y/D = 10$. The spanwise domain size of the LES and RANS is $z/D = 1.2$. The grid is uniform in the spanwise direction and periodic boundary conditions are used on the spanwise boundaries. To ensure a fully developed boundary layer a transition length of approximately three boundary-layer thicknesses is required by the RSTG approach. Since the boundary-layer thickness directly upstream of the base shoulder is $\delta = 0.15D$, the LES inflow plane is positioned at $x/D = -0.5$ to guarantee a fully developed turbulent boundary layer upstream of the BFS geometry. The LES inflow plane inside the nozzle is located at $x/D = 0.95$.

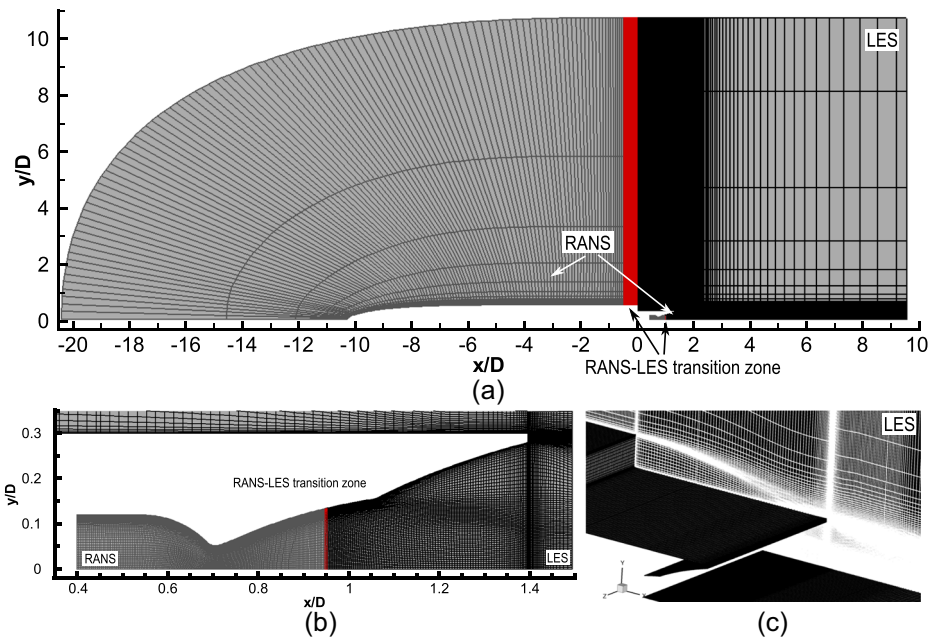


Fig. 3 (a) Overview of the zonal grid topology; (b) zonal grid for the nozzle region; (c) LES grid for the wake zone

Table 2 Number of mesh points in each direction for the respective domains

	N_x	N_y	N_z	Σ
RANS (forebody)	481	133	17	$1.1 \cdot 10^6$
RANS (nozzle)	1027	222	5	$1.1 \cdot 10^6$
LES (main body)	209	97	801	$16.2 \cdot 10^6$
LES (near wake)	339	177	801	$48.0 \cdot 10^6$
LES (nozzle)	355	247	801	$70.2 \cdot 10^6$
LES (far wake)	429	499	801	$171.5 \cdot 10^6$
Total				$308 \cdot 10^6$

The characteristic grid resolution in the area within the transition zone in inner wall units $l^+ = u_\tau/\nu$ is $\Delta x^+ = 50$, $\Delta y^+ = 2$, and $\Delta z^+ = 30$ for the LES zone and $\Delta x^+ = 350$, $\Delta y^+ = 1$, and $\Delta z^+ = 1500$ for the RANS domain. The resolution is chosen according to typical mesh requirements in wall-bounded flows outlined by Choi & Moin [28] and is based on previous investigations [12, 19] showing the resolution to be sufficient. In total 308 million grid points are used for the zonal setup. The number of grid points in each direction for the respective domains are listed in Table 2.

2.4 Modal decomposition

To separate large-scale coherent flow patterns from the turbulent background of the complex wake and nozzle flow, modal decomposition methods, i.e., POD and DMD, are applied in the present study. POD and DMD are data-driven decomposition techniques that in contrast to model-based approaches offer the advantage that no information about the underlying, mostly nonlinear and high-dimensional dynamical system is needed. Besides the identification of characteristic structures like large scale vortices being of particular importance to the underlying flow field, the extracted modes can serve as a basis for a reduced-order model, thus the original dynamical system can be projected onto a model system with fewer degrees of freedom.

2.4.1 Proper orthogonal decomposition

In the proper orthogonal decomposition technique the flow field is decomposed into spatially orthogonal modes with multi-frequency temporal content based on optimizing the mean square of the examined flow variable. The high-dimensional flow field data at the discrete time step t_n is given by the vector field $\mathbf{q}(\mathbf{x}, t_n)$, $\mathbf{x} \in \mathbb{R}^M$. In the present study, the fluctuating component of the flow field data is used for the POD analysis. The Reynolds decomposition yields $\mathbf{q}(\mathbf{x}, t_n) = \bar{\mathbf{q}}(\mathbf{x}) + \mathbf{q}'(\mathbf{x}, t_n)$, where $\bar{\mathbf{q}}(\mathbf{x})$ is the temporal averaged and $\mathbf{q}'(\mathbf{x}, t_n)$ the fluctuating component of the flow data. The three-dimensional data is rearranged into a single data vector ψ_n for each time step t_n and assembled in the snapshot matrix $\Psi = [\psi_1 \ \psi_2 \ \dots \ \psi_N]$ including all time steps. The POD modes are determined by solving the eigenvalue problem

$$\mathbf{R}\phi_m = \lambda_m\phi_m, \quad \lambda_1 \geq \dots \geq \lambda_m \geq 0, \quad (3)$$

where

$$\mathbf{R} = \sum_{n=1}^N \psi_n \psi_n^T = \boldsymbol{\psi} \boldsymbol{\psi}^T$$

is the autocorrelation matrix. The eigenvectors ϕ_m are the spatial POD modes which define an orthonormal basis and the eigenvalues λ_m represent the contribution of each mode to the total fluctuating energy. It is assumed that the most energetic modes are the relevant modes containing the bulk of momentum in the flow. To calculate the temporal coefficient of each mode, the original snapshots are projected onto the POD basis

$$a_m(t_n) = \langle \psi_n, \phi_m \rangle = \int_V \psi_n \cdot \phi_m dV. \tag{4}$$

Based on the spatial POD modes and temporal coefficients the initial flow field can be reconstructed according to the following equation

$$\psi_n = \sum_{m=1}^M a_m(t_n) \phi_m. \tag{5}$$

A more detailed description of the mathematical background of POD is given in Berkooz et al. [29] and Taira et al. [30].

2.4.2 Dynamic mode decomposition

DMD is based on the Koopman operator to determine a basis of non-orthogonal spatial modes each associated with a specific constant frequency from a multi-dimensional data field obtained from time-resolved experiments or simulations. While the POD modes exhibit a multi-frequency temporal content and are arranged according to their energy content, potentially missing dynamically highly relevant but low-energy modes, DMD provides single frequency modes which are assessed based on their dynamical importance. The DMD algorithm used in the present study was initially developed by Schmid [31], including an economy-sized singular value decomposition (SVD) to guarantee a more robust calculation in case of an ill-conditioned input dataset. As usual for data-driven techniques, the DMD algorithm requires a sequence of equidistantly sampled snapshots arranged in form of the data matrix $\boldsymbol{\psi} = \{\psi_0, \psi_1, \dots, \psi_N\}$, where $\psi_n := \psi(x, y, z, t_n)$ represents the high-dimensional flow field at the discrete time step t_n . The DMD algorithm projects the data matrix onto a set of non-orthogonal spatial modes

$$\underbrace{[\psi_0 \ \psi_1 \ \dots \ \psi_{N-1}]}_{\boldsymbol{\psi}_0} \approx \underbrace{[\phi_1 \ \phi_2 \ \dots \ \phi_N]}_{\boldsymbol{\Phi}} \cdot \underbrace{\begin{pmatrix} a_1 & & & \\ & a_2 & & \\ & & \ddots & \\ & & & a_N \end{pmatrix}}_{D_a = \text{diag}\{a\}} \underbrace{\begin{pmatrix} 1 & \mu_1 & \dots & \mu_1^{N-1} \\ 1 & \mu_2 & \dots & \mu_2^{N-1} \\ \vdots & \vdots & \ddots & \vdots \\ 1 & \mu_N & \dots & \mu_N^{N-1} \end{pmatrix}}_{V_{and}}. \tag{6}$$

The quantity ϕ_n represents the spatial modes, a_n the amplitude of the corresponding DMD mode, and V_{and} the Vandermonde matrix containing the eigenvalues μ_n , which determine the temporal evolution, i.e., the frequencies and decay rates of the modes. To determine the unknown amplitudes a_n the following convex optimization problem is solved

$$\underset{a}{\text{minimize}} \ \|\boldsymbol{\psi}_0 - \boldsymbol{\Phi} D_a V_{and}\|_F^2. \tag{7}$$

This means that the amplitudes are chosen such that the entire input data sequence is optimally approximated. To reconstruct the temporally developing flow field the entire or a subset of the DMD modes can be superimposed according to the following equation

$$\psi(x, y, z, t) = \sum_{n=1}^N a_n e^{(\lambda_n t)} \phi_n(x, y, z). \quad (8)$$

The quantity λ_n is the complex frequency which is determined by

$$\lambda_n = \frac{\log(\mu_n)}{\Delta t} = \underbrace{\frac{\ln|\mu_n|}{\Delta t}}_{D_n} + i \cdot \underbrace{\arctan\left(\frac{\mu_{n,imag}}{\mu_{n,real}}\right)}_{\omega_n} \frac{1}{\Delta t}, \quad (9)$$

where the real part D_n is the decay rate and the imaginary part ω_n is the angular frequency of the respective mode.

To select the DMD modes capturing the most important dynamic structures the sparsity-promoting algorithm introduced by Jovanovic et al. [32] is applied. Within the algorithm sparsity is induced by adding an additional term to the objective function in Eq. 7 that penalizes the l_1 -norm of the vector of the DMD amplitudes. The following optimization problem is obtained

$$\underbrace{\text{minimize}}_a \|\psi_0 - \Phi D a\|_F^2 + \gamma \sum_{i=1}^N |a_i|, \quad (10)$$

where the positive regularization parameter γ specifies the relative emphasis on the sparsity of the vector a . The quantity γ can be used to trade the approximation error with respect to the full data against the number of extracted modes.

The DMD algorithm is parallelized using MPI and ScaLAPACK to handle the large amount of data, the I/O is performed using the HDF5 parallel file format. For a more detailed description of the DMD algorithm, the reader is referred to Schmid [31] and Jovanovic et al. [32].

3 Results

The discussion of the results is divided into three parts. First, the general characteristics of the wake flow topology plus dual-bell nozzle flow is presented, compared to the results of the previously investigated configuration with a classical TOP nozzle and validated by experimental data. Subsequently, the dynamic behavior of the outer wake flow is investigated by classical statistical analysis, POD, and DMD to detect spatio-temporal modes which are responsible for the pressure loads on the outer nozzle surface. Finally, the dynamic behavior of the dual-bell nozzle flow characterized by the separation at the contour inflection and the consequent entrainment of the outer flow into the nozzle extension is investigated by spectral methods, POD, and DMD.

3.1 Wake flow topology and validation

The overall flow topology is visualized by the instantaneous distribution of the Mach number and the pressure coefficient around the generic space launcher shown in Fig. 4. In Fig. 5 a zoom of Fig. 4 emphasizing the flow in the near wake and the nozzle and an instantaneous numerical pseudo-schlieren picture of the wake flow are given. The incoming freestream

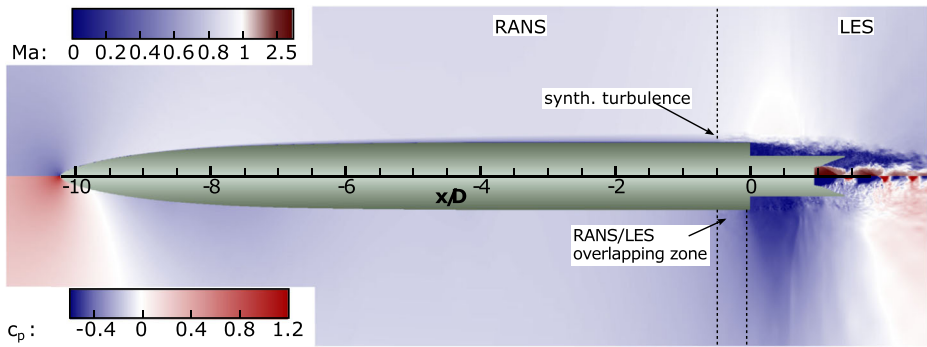


Fig. 4 Flow topology of the generic planar space launcher configuration: Instantaneous Mach number distribution (top); pressure coefficient (bottom)

with a Mach number of $Ma_\infty = 0.8$ accelerates along the launcher’s nose to a local maximum of $Ma \approx 0.92$ and decelerates again to $Ma \approx 0.87$ around the main body. At the abrupt junction between the main body and the nozzle fairing, the incoming turbulent boundary layer separates and a turbulent free-shear layer emanates. Due to the low base pressure in the separation region, the flow strongly accelerates towards the BFS forming a local supersonic region. Inside the dual-bell nozzle, the flow accelerates to $Ma \approx 2.8$ and separates at the contour inflection forming classical shock cells, which are expected since the nozzle pressure ratio is below the transition pressure ratio.

Figure 6 shows the time-averaged streamwise velocity contours and streamlines and the instantaneous distribution of the spanwise vorticity component for the dual-bell nozzle configuration and the reference configuration with the conventional TOP nozzle. First, the wake flow topology of the dual-bell nozzle setup is discussed, followed by a comparison of the two configurations. At the abrupt junction between the main body and the nozzle, the incoming turbulent boundary layer separates. The shed shear layer continuously broadens due to shear layer instabilities causing the initially small turbulent structures to grow in size and intensity similar to structures observed in the planar free-shear layers by Winant & Browand [33]. Further downstream, the structures either impinge on the surface approximately between $0.8 < x/D < 1.4$ or pass downstream without interacting with the nozzle

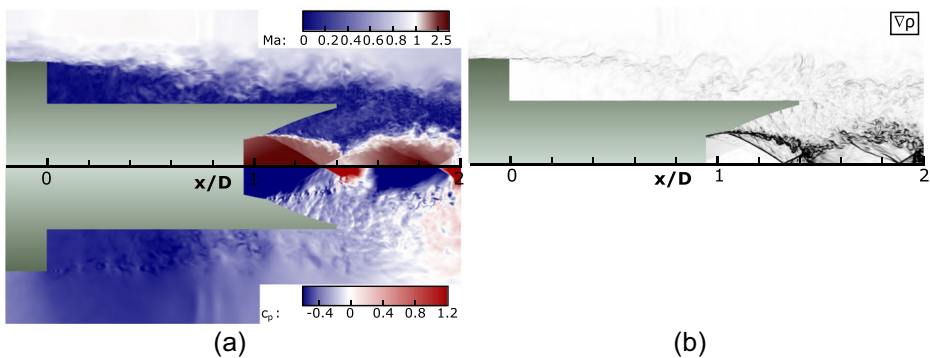


Fig. 5 Zoom of the instantaneous Mach number and pressure distribution in the near wake and the nozzle (a). Instantaneous numerical pseudo-schlieren picture ($|\nabla\rho|$) (b)

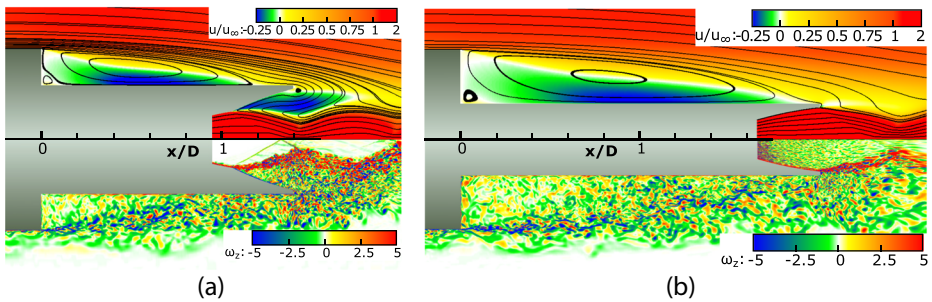


Fig. 6 Flow topology: Time and spanwise averaged streamwise velocity contours and streamlines (top); instantaneous distribution of the spanwise vorticity component in the center cross-section at $z/D = 0.6$ (bottom): (a) Dual-bell nozzle configuration, (b) TOP nozzle configuration

surface. Downstream of the base, a large low pressure recirculation region occurs. In the dual-bell nozzle, the turbulent boundary layer separates at the contour inflection and shock cells are formed. In the nozzle extension, a backflow region forms entraining the eddies of the outer flow into the nozzle where they interact with the jet plume. Due to this interaction and the strong shear of the mean flow field between the backflow area and the jet, intensive turbulent structures are generated inside the nozzle extension. Due to the manifold of turbulent structures, a straightforward interpretation of the instantaneous flow field is quite complicated. Therefore, POD and DMD are used in the following sections to identify the underlying coherent motion of the wake and the nozzle flow dynamics. The overall topology of the outer wake flow, i.e., the shear layer development and recirculation region is comparable to the TOP nozzle configuration. The time averaged reattachment position is $x/D = 1.2$ for the dual-bell nozzle case and $x/D = 1.9$ for the reference configuration. Taking into account the different step heights, the time averaged reattachment length is almost identical. However, due to the entrainment of the outer flow into the nozzle and the strong shear caused by the flow separation and backflow inside the nozzle extension, the turbulent fluctuations around the plume are substantially enhanced in the dual-bell nozzle configuration.

To investigate the influence of the dual-bell nozzle onto the pressure distribution along the launcher's surface, the wall-pressure p/p_∞ of the fully coupled RANS/LES simulation is shown as a function of the streamwise position for the dual-bell and TOP nozzle configuration in Fig. 7. Due to the local acceleration along the nose, the pressure initially drops to a local minimum of $p/p_{inf} = 0.9$ and increases again as the flow decelerates along the

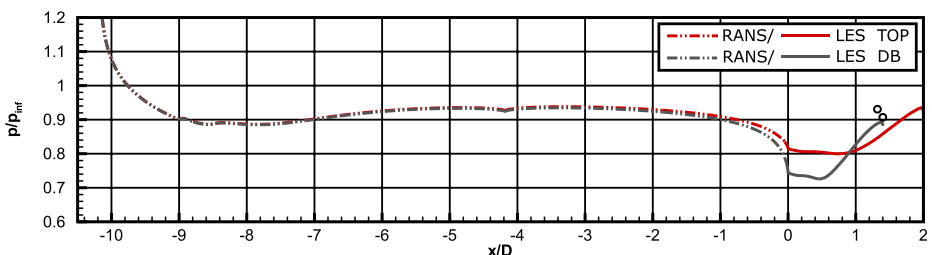


Fig. 7 Streamwise distribution of the mean wall-pressure; comparison of the dual-bell nozzle and TOP nozzle configurations

forebody. On the first half of the nozzle extension at $0 < x/D < 0.6$, the pressure coefficient exhibits a plateau-like minimum with a constant value of $p/p_{inf} = 0.74$, followed by a quasi linear increase near the end of the nozzle which is caused by the impinging shear layer. The low base pressure exhibits a significant upstream influence on the attached boundary layer around the forebody. The flow accelerates already upstream of the shoulder leading to a decreasing pressure coefficient. This is taken into account in the simulation due to the full bidirectional coupling of the zonal method enabling an upstream propagation of the information from the LES to the RANS zone. The comparison between the two cases shows a qualitatively similar development of the wall pressure along the launcher's surface. The absolute pressure level in the recirculation region, however, is decreased in the dual-bell nozzle configuration, which is due to the shorter nozzle length increasing the suction effect of the high streamwise momentum of the supersonic plume and a lower pressure level at the nozzle lip. The pressure increase towards the nozzle end is located further upstream in the dual-bell nozzle configuration since the reattachment length normalized by the launcher's thickness is smaller. The lower base pressure reduces the wall pressure up to the center of the forebody. This result also shows the necessity of the bidirectional coupling between the LES and the RANS zones.

The streamwise distribution of the root-mean-square (rms) coefficient of the pressure fluctuations $c_{prms} = \overline{p'^2}/q_\infty$ on the outer nozzle surface is given for the two configurations in Fig. 8. Both distributions exhibit a small local extremum just downstream of the backward facing step at $x/D = 0.15$ and $x/D = 0.2$ which is caused by the secondary recirculation region. Further downstream, the rms values steadily increase in the streamwise direction, reach their maximum around the reattachment position, and slightly decrease toward the nozzle end. The increase in the pressure fluctuations around the reattachment position is generated by the vortical structures in the shear layer impinging on the nozzle surface. Note that the streamwise position, where the rms value starts to strongly increase, i.e., at $x/D \approx 0.45$ and $x/D \approx 0.8$, coincides with the location of the mean pressure recovery in Fig. 7. While the overall distribution of the compared configurations is quite similar, the increase is located further upstream in the dual-bell case, since the step height and consequently the reattachment length is decreased. Since the maximum value at the end of the nozzle extension is comparable, the novel nozzle concept seems not to effect the dynamic loads onto the outer nozzle fairing.

To evaluate and compare the pressure fluctuations in the whole wake flow field, the rms pressure coefficient is depicted in Fig. 9 for the two configurations. The development of the

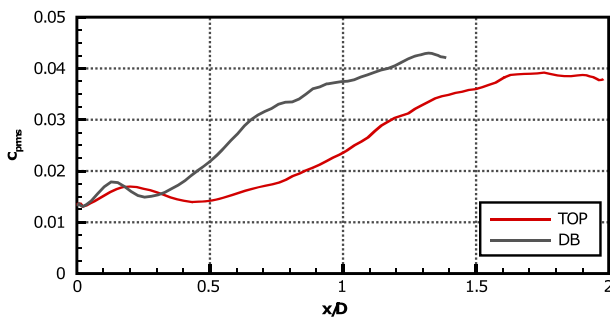


Fig. 8 Streamwise distribution of the root-mean-square wall-pressure coefficient along the outer nozzle fairing; comparison of the dual-bell nozzle and TOP nozzle configurations

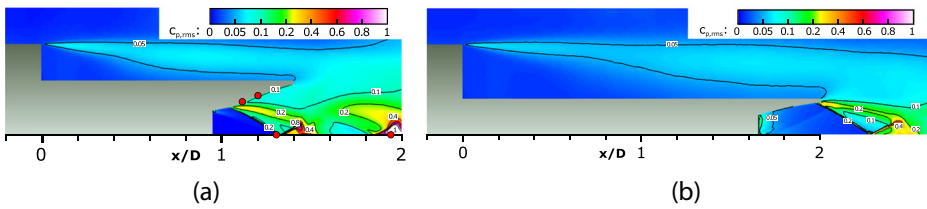


Fig. 9 Spanwise averaged root-mean-square wall-pressure coefficient contour; comparison of the (a) dual-bell nozzle and (b) TOP nozzle configurations. The red dots mark the pressure measurement positions used in Section 3.3.1

outer shear layer and the generated fluctuations is quite similar, as already indicated from the wall pressure fluctuations. Around the shock cells, which develop downstream of the nozzle, the pressure fluctuations are significantly increased compared to the TOP nozzle configuration, reaching values twice as high. Since the shock originates from the separation at the contour inflections, the enhanced fluctuations produce increased dynamic loads on the wall of the nozzle extension.

To validate the zonal RANS/LES computation, the obtained temporal averaged flow field is compared to experimental investigations performed at the Bundeswehr University Munich [20]. It is worth mentioning that the planar wind tunnel model only features a dual-bell nozzle in the mid 20% percent of the total span while the rest is designed as a nozzle fairing without a jet. Due to wind tunnel limitations, the outer stagnation pressure was larger leading to an approximately 9% reduced nozzle pressure ration compared to the numerical setup. The static pressure measured shortly upstream of the nozzle lip, i.e., $x/D = 1.3$, $y/D = 0.3$ and at the nozzle lip, i.e. $x/D = 1.2$, $y/D = 0.25$, is presented along with the numerical pressure distribution in Fig. 7. Since the nozzle lip is extremely small, the pressure is measured in a x - y plane in the area of the jetless nozzle faring at a spanwise position that is $0.64D$ away from the section with the dual-bell nozzle. Taking into account the mentioned differences, the experimental and numerical results exhibit a very good agreement. Profiles of the mean streamwise velocity distribution normalized with the respective freestream velocity upstream of the BFS are given for four streamwise positions in the center cross-section in Fig. 10a. The experimental shear layer position is

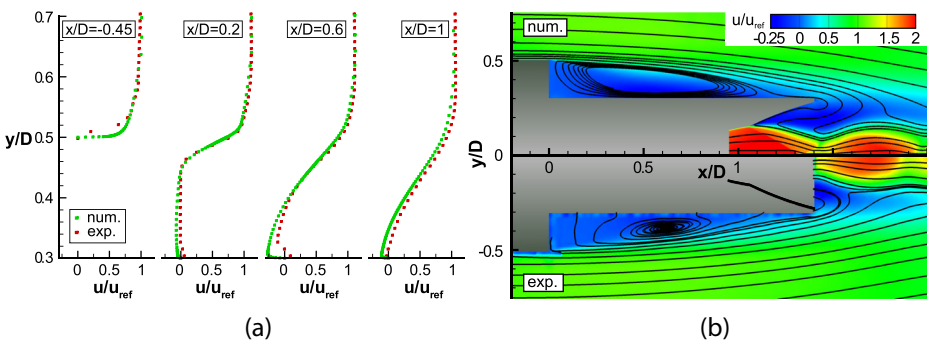


Fig. 10 Validation of the dual-bell nozzle configuration: (a) Time averaged streamwise velocity profiles at four streamwise positions upstream and downstream of the BFS. (b) Numerical (top) and experimental (bottom) time averaged streamwise velocity contours and streamlines

closely matched by the numerical results. Only in the vicinity to the outer nozzle wall, the experimental maximum backflow velocity in the recirculation region is lower compared to the numerical results. However, this is likely caused by measurement errors caused by laser-light reflections at the model surface. In Fig. 10b the numerical and experimental streamwise velocity contours and streamlines in the center cross-section are comparatively juxtaposed. The overall flow topology, i.e., the recirculation region and the reattachment length is in very good agreement. Merely small differences are apparent in the shape of the plume which are, however, related to the smaller nozzle pressure ratio in the experiments leading to a further upstream located shock pattern. To sum up, the comparison with the experimental results displays a good agreement demonstrating the capability of the numerical approach to accurately reproduce the investigated flow field.

The spanwise vorticity distribution in Fig. 6a shows that the turbulent wake of the planar space launcher configuration is characterized by the interaction of a large number of structures exhibiting various time and length scales. The strong time dependence of the wake is also evident in the upper illustrations in Fig. 11 showing the instantaneous streamwise velocity distribution and streamlines in the cross-section at $z/D = 0.9$ at two time instants. At $t = t_0$ the recirculation region is relatively small leading to an impingement of the shear layer on the nozzle surface in the range of $0.7 < x/D < 0.9$ which is more than $0.3D$ upstream of the time averaged reattachment position. Later at $t + \Delta t$ the recirculation region is greatly enlarged and the free-shear layer passes over the nozzle hardly interacting with it. This oscillation of the recirculation region and consequently, the variation of the impingement location are characteristic for the separating-reattaching flow past a BFS. Despite the straight separation line defined by the edge at the BFS, the recirculation region and the shear layer exhibit a strong spanwise variation leading to an alteration of the streamwise impingement location depending on the spanwise position. This is illustrated by the instantaneous

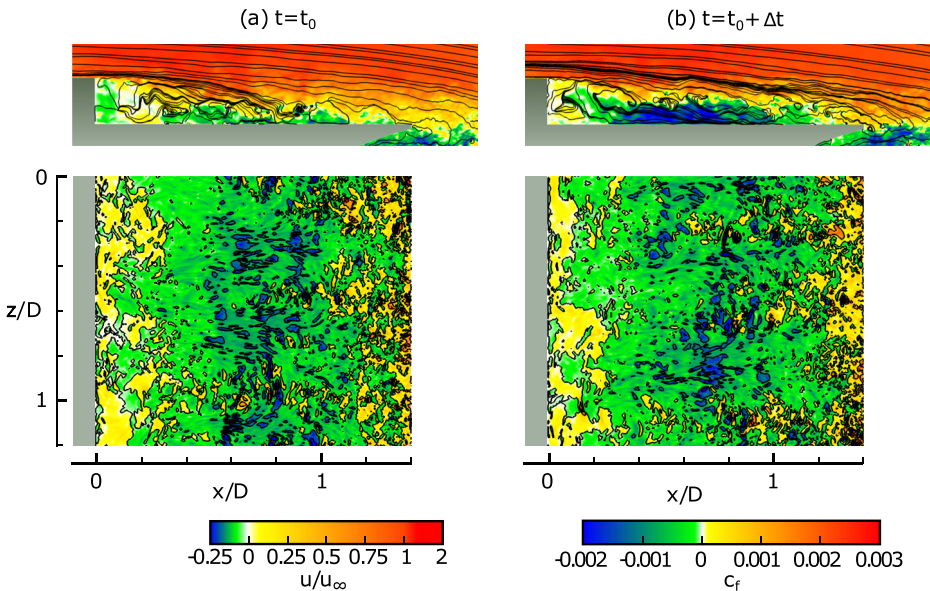


Fig. 11 Instantaneous wake flow at two time steps: Streamwise velocity distribution and streamlines in the wake (top); skin-friction coefficient distribution on the nozzle surface (bottom)

distribution of the skin-friction coefficient on the nozzle surface in Fig. 11. The skin-friction coefficient distribution exhibits wedge-shaped reattachment regions with a spanwise wavelength of approximately $\lambda/D = 0.4$ ($\lambda/h = 2$) which alternate their spanwise position over time. A similar time-dependent behavior was observed in pure BFS configuration [12, 13] and in the previous investigation with the TOP nozzle [21]. That is, the integration of the dual-bell nozzle seems to not effect the overall dynamics of the flow around the nozzle fairing.

3.2 Analysis of the wake dynamics

3.2.1 Temporal spectral analysis

To evaluate the temporal periodicity of the wake dynamics and the resulting dynamic loads, the power spectral density (PSD) of the wall pressure fluctuations is discussed in the following. The PSD computation is based on a sequence of 3072 time instants equidistantly sampled with $\Delta t = 0.1t_{ref}$ with $t_{ref} = D/u_\infty$. Welch's algorithm with Hanning windows of 512 samples each and an overlap of 50% is used. Hence, according to the Nyquist criterion frequencies in the range of $1.95 \cdot 10^{-2} < Sr_D < 5$ can be determined. To improve the statistical quality of the results, the PSD is computed for 401 points equidistantly distributed in the spanwise direction and subsequently averaged in the frequency space.

The resulting premultiplied normalized PSD spectra at two streamwise positions are given in Fig. 12a. At $x/D = 0.3$ the spectrum reveals three distinct peaks at $Sr_D = 0.045$, $Sr_D = 0.14$ and $Sr_D = 0.24$, where Sr_D is the Strouhal number based on the launcher's thickness D and the freestream velocity u_∞ . At the position further downstream, i.e., $x/D = 1$, the peak at $Sr_D = 0.24$ is also apparent. Besides the narrow, lower frequency peaks, a broadband range at higher frequencies with a maximum at $Sr_D = 3$ for $x/D = 0.3$ and $Sr_D = 0.7$ for $x/D = 1$ resulting from the vortical structures within the separated shear layer is visible. The maximum is located at a higher frequency for the position further upstream due to the still smaller size of the vortical structures.

To understand the underlying flow phenomena leading to the undesired low frequency loads, a proper orthogonal decomposition and dynamic mode decomposition of the outer wake flow is conducted to extract dominant spatio-temporal modes from the time resolved three-dimensional flow field and to reduce the complex flow physics to a few degrees of freedom.

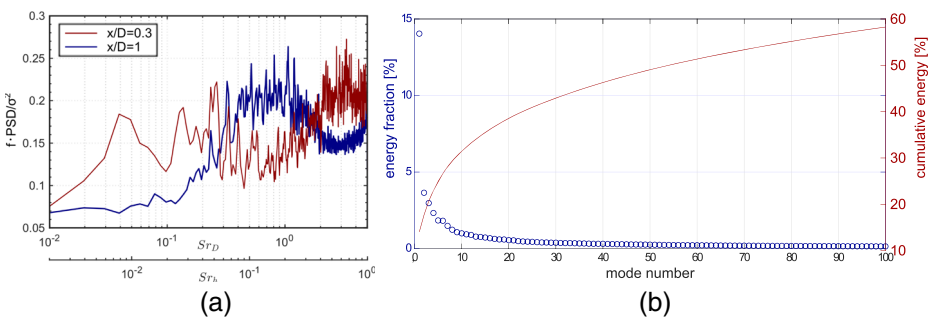


Fig. 12 (a) Power spectral density of the wall pressure fluctuations p'/p_∞ at $x/D = 0.3$ and $x/D = 1$. (b) Energy distribution over the POD modes

3.2.2 Modal analysis

The POD modes are computed using 3072 snapshots of the pressure and velocity field in the center cross-section, i.e., at $z/D = 0.6$. The snapshots are equidistantly distributed in time with $\Delta t = 0.1t_{ref}$. For the analysis, the mean flow field is subtracted from the instantaneous snapshot, i.e., only the fluctuation part of the pressure and velocity field is used. The energy fractions of the POD modes are given in Fig. 12b. The first hundred modes possess a cumulative energy of about 60% showing that the flow is characterized by large-scale coherent motion. The motion described by the first mode containing 14% of the total energy and the second mode with 4% of the energy is discussed in the following to explain the dynamic behavior previously outlined.

The spatial shape of the first mode ϕ_1 is illustrated in Fig. 13a by the streamwise and wall-normal velocity component. To visualize the impact of the mode onto the wake flow, the original snapshots are additionally conditional averaged based on the time coefficient of the first mode. That is, two subgroups of the original snapshots are defined and averaged in time. In the first group, the time instants corresponding to the largest 10% of the time coefficient and in the second group, corresponding to the smallest 10% of the time coefficient are collected. The two resulting averaged flow fields are shown by means of the streamwise velocity contours and streamlines in Fig. 13b. The first POD mode exhibits a local minimum in the streamwise velocity component and a local maximum in the wall-normal velocity component near the time averaged shear layer location. Superposing the two velocity components results in a movement of the shear layer towards the wall and in the upstream direction, i.e., to a contraction of the separation bubble. This is also evident from the first conditional averaged flow field (Fig. 13b, top) exhibiting a substantial reduced recirculation region and reattachment length. When the sign of the amplitude is reversed, the first mode will result in an enlargement of the recirculation region as visible in the second conditional averaged flow field (Fig. 13b, bottom). Consequently, the dynamics seen in the instantaneous streamline snapshots shown in the previous section can be associated to this first POD mode. This periodic growing and contracting of the separation bubble was

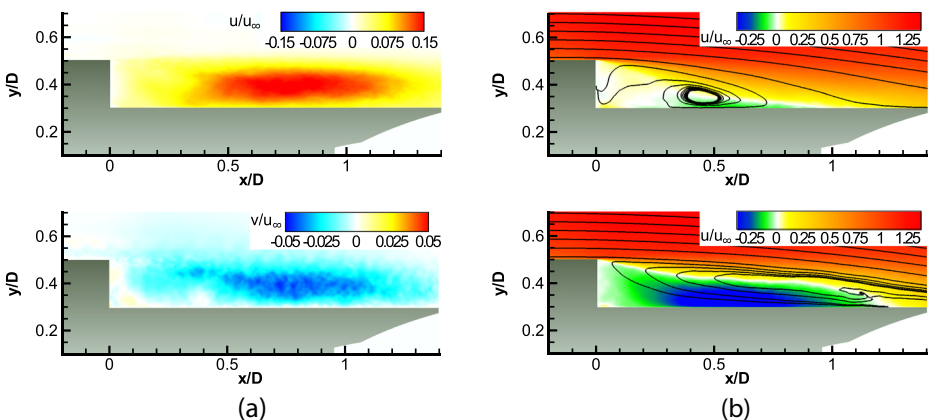


Fig. 13 Visualization of the POD mode ϕ_1 : (a) Streamwise velocity distribution (top); wall-normal velocity distribution (bottom). (b) Conditional averaged streamwise velocity contours and streamlines, max 10% (top), min 10% (bottom)

also observed by Schrijer et al. [17] in an axisymmetric configuration and Driver et al. [7] in a 2D-BFS flow and is commonly called shear-layer “flapping”.

In Fig. 14, the same quantities are plotted for the second POD mode ϕ_2 . The streamwise and the wall-normal velocity distribution exhibit two local extrema. At the first extremum at $x/D \approx 0.7$, the streamwise velocity component is negative and the wall-normal velocity component is positive. At the second extremum at $x/D \approx 1.2$, the signs are opposite. The combination of both velocity components leads to an upward and downstream directed shift of the shear layer at the first and an opposite shift at the second extremum. Therefore, the second mode describes an oscillating wavy motion of the shear layer, as clearly apparent from the two conditional averaged flow fields given in Fig. 14b. A comparable undulating motion of the shear layer was detected by a POD analysis of the wake flow of an axisymmetric space launcher configuration [17]. The motion is ascribed to large-scale structures inducing momentum injection into the recirculation bubble upstream and momentum ejection out of the recirculation bubble downstream of the reattachment location.

To finalize the analysis of the wake dynamics and to extract potentially dynamically highly important modes containing only a small amount of energy, consequently being neglected in the POD analysis, DMD is applied to the three-dimensional wake flow. The dynamic mode decomposition is performed using $N = 512$ samples of the three-dimensional velocity and pressure field of the wake. The samples are equidistantly distributed with a frequency of $Sr_D = 10$. To save computational costs, the spatial resolution is reduced by using only every second point in the wall normal direction and every fourth point in the spanwise direction. The resulting DMD spectrum is shown in Fig. 15. The complex DMD eigenvalues μ_n are plotted together with the unit circle to enable the assessment of the decay rates. The amplitudes a_n of the DMD modes normalized by the amplitude a_{mean} of the mean mode and multiplied by the respective damping $|\mu_n|^N$ are shown as a function of their dimensionless frequency $Sr_D = Im(\lambda_n) / (2\pi \Delta t)$. The multiplication by the damping factor reduces the amplitudes of transient modes which immediately decay and consequently are of minor importance for the overall flow dynamics. The selection of the important modes is based on the sparsity-promoting approach by Jovanovic et al. [32]. The three most stable modes, i.e., $Sr_{D,1}(\lambda_1) = 0.047$, $Sr_{D,2}(\lambda_2) = 0.147$, and $Sr_{D,3}(\lambda_3) = 0.249$, are identified

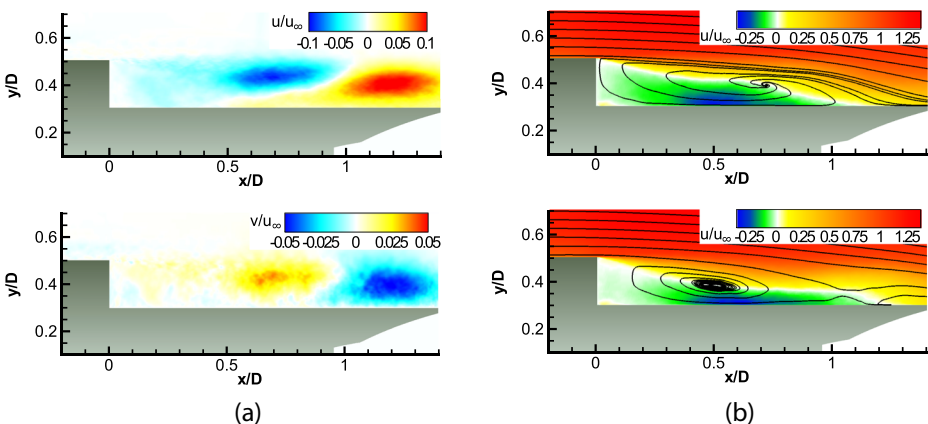


Fig. 14 Visualization of the POD mode ϕ_2 : (a) Streamwise velocity distribution (top); wall-normal velocity distribution (bottom). (b) Conditional averaged streamwise velocity contours and streamlines, max 10% (top), min 10% (bottom)

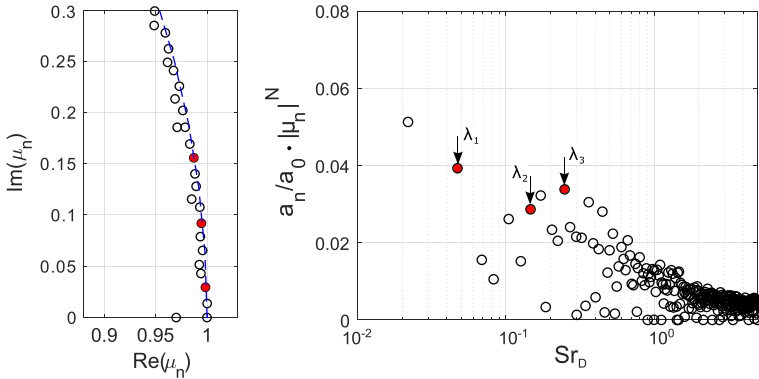


Fig. 15 Normalized DMD spectrum of the three-dimensional velocity and pressure field; eigenvalues $\mu_n = e^{(\lambda_n \Delta t)}$ (left), normalized amplitude distribution versus frequencies $\mathfrak{S}(\lambda_n)$ (right)

and marked by red filled circles. The dimensionless frequencies of these modes coincide with the characteristic frequencies of the PSD spectra of the pressure fluctuations shown in Fig. 12a.

To visualize the three-dimensional shape and temporal evolution of the identified DMD modes, the spatial modes ϕ_n are superimposed with the mean mode ϕ_{mean} and reconstructed in time according to Eq. 8. The resulting flow field is given for the first two modes at two time instances in Figs. 16 and 17.

The low frequency mode ϕ_1 describes a periodic enlargement and contraction of the recirculation bubble in the streamwise direction coinciding with the energy richest POD mode. Besides the oscillation in the streamwise direction, the recirculation region also strongly alternates in the spanwise direction forming wavy structures changing their spanwise position over time. Therefore, this coherent motion explains the wedge-shaped reattachment regions detected in the skin-friction distribution. A similar spatio-temporal mode was found in previous investigations of the planar configuration with the conventional nozzle [21] and in a pure BFS configuration [12] and denoted as “cross-pumping” mode due to the combined longitudinal pumping motion and the strong alteration in the spanwise direction.

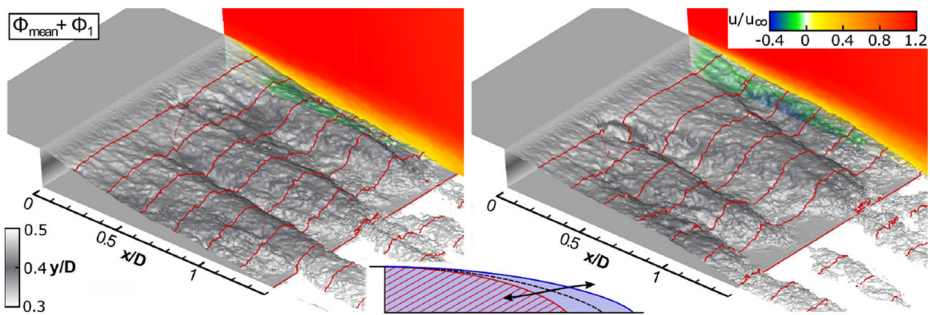


Fig. 16 Reconstruction of the DMD mode ϕ_1 at two time instances. The recirculation region is visualized by a contour for the streamwise velocity at $u/u_\infty = 0.1$ colored by the distance from the nozzle surface

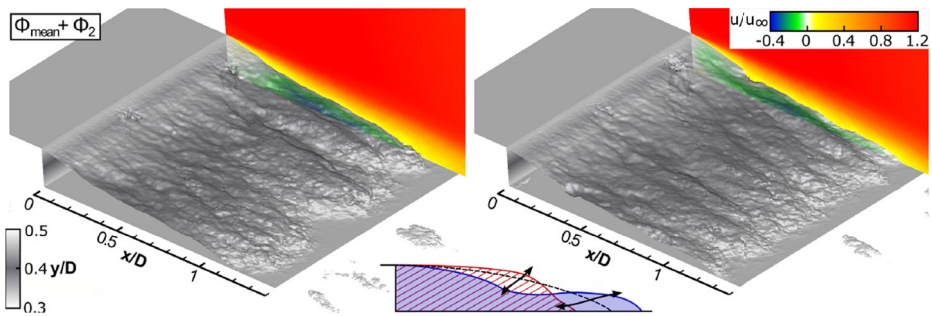


Fig. 17 Reconstruction of the DMD mode ϕ_2 at two time instances. The recirculation region is visualized by a contour for the streamwise velocity at $u/u_\infty = 0.1$ colored by the distance from the nozzle surface

The second DMD mode describes a wave-like undulating motion of the shear layer similar to the second POD mode which can be associated to large-scale spanwise rotational structures. In addition, like the low frequency mode, the second mode has a pronounced three-dimensional shape. The third mode also depicts a wave-like oscillating motion of the shear layer that is very similar to the second mode and therefore, the mode is not shown here. Analogous modes were also observed in the previous investigation of the planar configuration with the conventional nozzle [21] and in an axisymmetric configuration [19]. In addition, the coherent motion captured by the second and third stable mode is similar to the high frequency “cross-flapping” motion discovered in the investigation on the pure BFS configuration [12].

In summary, the modal decomposition of the outer wake flow indicates that the dynamic behavior of the wake and consequently, the dynamic pressure loads on the outer nozzle fairing are caused by a growing and contracting separation bubble and an undulating motion of the shear layer. The detected modes match the modes of the reference configuration with the conventional TOP nozzle [21] showing that the dynamics of the recirculation bubble downstream of the BFS is not affected by the dual-bell nozzle.

3.3 Analysis of the nozzle flow dynamics

3.3.1 Temporal spectral analysis

The results discussed in Section 3.1 reveal that the pressure fluctuations in the plume and on the inner wall of the dual-bell nozzle extension are increased compared to the TOP nozzle setup. To investigate the flow dynamics leading to the increased pressure loads and to analyze the temporal periodicity of those pressure loads, the PSD of the pressure fluctuations is computed at several positions which are indicated by red dots in Fig. 9. The PSD is based on 3072 time samples which are sampled with $\Delta t = 0.1t_{ref}$. The data is analyzed using Welch’s algorithm with Hanning windows comprising 512 samples each and an overlap of 50%. Exploiting the quasi two-dimensional configuration the spectra are averaged in the spanwise direction using 401 equally distributed spanwise positions. On the left of Fig. 18, the spectra of the wall pressure fluctuations at two streamwise positions at the nozzle extension and on the right, the spectra at two locations on the centerline, i.e., $y/D = 0$, are shown. On the nozzle wall and centerline one main peak with a Strouhal number of $St_D = 0.61$ and two slightly weaker peaks with a Strouhal number of $St_D = 0.4$ and $St_D = 0.9$ are prominent features of the distributions. The results indicate that a specific

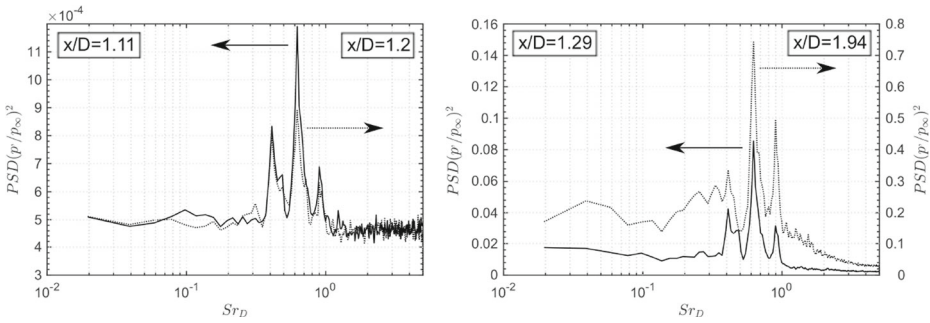


Fig. 18 Power spectral density of the pressure fluctuations p'/p_∞ on the nozzle wall (left) and on the centerline (right) at different streamwise positions

periodic flow phenomenon is causing the increased pressure loads in the jet region. To identify the coherent motion leading to the periodic pressure signal, further analyses based on POD and DMD have to be carried out.

3.3.2 Modal analysis

First, the POD analysis of the flow that encompasses the nozzle and the jet is shown. The modal decomposition is based on the evaluation of 3072 snapshots of the pressure and velocity field in the x - y plane in the center of the spanwise domain length, i.e., at $z/D = 0.6$ equidistantly distributed in time with $\Delta t = 0.1t_{ref}$. Note that only the fluctuation part of the pressure and velocity is used for the analysis. The distribution of the streamwise and vertical component of the first two most energetic POD modes are given in Fig. 19a and b. The amount of energy captured by the first mode is 6% and of the second mode 3% of the total energy. The first POD mode exhibits local regions with a negative streamwise velocity around the mean location of the shear layer shedding from the contour inflection and at the position of the primary and reflected shock. The v -velocity distribution has a negative sign at the position of the shock originating from the contour jump and a positive value at the reflected shock position. Superimposing both velocity components reveals that the first POD mode describes an oscillating variation of the shock angle, which is connected to a

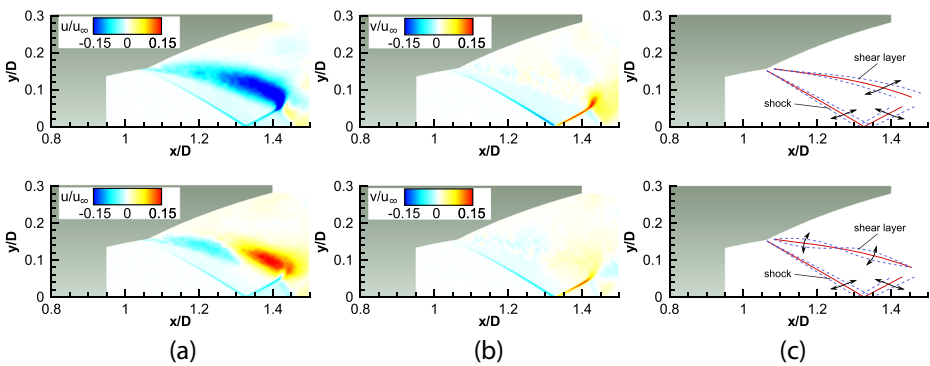


Fig. 19 Visualization of the first (top) and second (bottom) POD mode: (a) Streamwise velocity distribution; (b) wall-normal velocity distribution; (c) schematic illustration of the mode

streamwise pumping motion of the shear layer within the nozzle extension as illustrated in Fig. 19c, top. The streamwise velocity component of the second mode shows two local extrema with opposite signs located at the shear layer position and similar to the first mode an area with negative values around the shock position. The vertical velocity distribution is again characterized by a narrow region with negative velocities at the primary shock position and positive values around the reflected shock. Consequently, the second mode captures a wave-like motion of the shear layer again being connected to an oscillating motion of the shock wave as schematically shown in Fig. 19c, bottom.

Since the POD analysis is based on the temporally averaged spatial correlation tensor, the temporal information which is contained in the original snapshot data is not included in the POD modes. To retrieve information about the temporal content of the modes, the original snapshot data is projected onto the orthonormal basis given by the POD modes according to Eq. 4. To examine the relation of the POD modes with the previously discussed pressure loads, the temporal scales of the time coefficients are compared to the spectra of the pressure fluctuations. The PSD of the time coefficients of the first two POD modes is given in Fig. 20a. According to the analysis of the pressure fluctuations, the PSD function is calculated based on 3072 time samples equidistantly distributed with $\Delta t = 0.1t_{ref}$ using Welch's algorithm with Hanning windows of 512 samples and an overlap of 50%. In both modes distinct peaks at $Sr_D = 0.42$, $Sr_D = 0.61$ and $Sr_D = 0.9$ can be identified closely matching the characteristic frequencies detected in the spectra of the pressure fluctuations. To summarize the results of the POD analysis, the two most energetic modes describe an interaction of the separated shear layer insight the nozzle extension with the shock wave that leads to a streamwise oscillation of the shock and a pumping or wave-like motion of the shear layer. The results of the PSD of the temporal coefficients of the two POD modes show that the modes are linked to the pressure oscillations detected on the nozzle wall and centerline. Therefore, the motion captured by the POD modes is responsible for the increased pressure loads detected in the configuration with the dual-bell nozzle.

One of the known drawbacks of POD is the sorting of the modes depending on the amount of energy and not in terms of dynamical importance. Therefore, dynamically highly relevant but low-energy modes might be overseen by the POD analysis. To complete the analysis of the nozzle pressure fluctuations, a DMD analysis of the nozzle flow is performed and the extracted modes are compared to the POD modes. The DMD analysis is based on

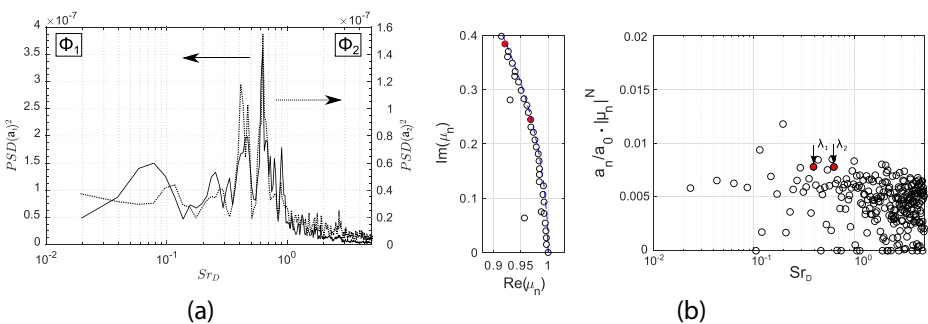


Fig. 20 (a) Power spectral density of the first and second POD mode coefficient. (b) Normalized DMD spectrum of the three-dimensional velocity and pressure field; eigenvalues $\mu_n = e^{(\lambda_n \Delta t)}$ (left), normalized amplitude distribution versus frequencies $\Im(\lambda_n)$ (right)

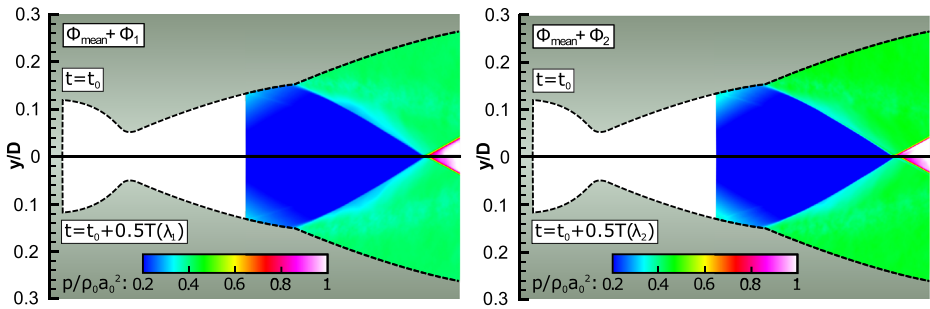


Fig. 21 Reconstruction of the DMD mode ϕ_1 (left) and ϕ_2 (right) at two time instances, visualized by pressure contours

512 snapshots of the three-dimensional velocity and pressure field inside the nozzle. The snapshots are sampled with $\Delta t = 0.1t_{ref}$.

The computed DMD spectrum is shown in Fig. 20b. On the left, the Ritz eigenvalues are plotted with respect to the unit circle to assess the temporal damping of the respective modes, on the right, the amplitudes are given as a function of the non-dimensional frequency $Sr_D(\lambda_n)$. Note that the amplitudes are again multiplied by the respective damping of the mode. To identify the important dynamic modes the sparsity-promoting algorithm by Jovanovic et al. [32] is applied. The two most relevant modes detected by the sparsity-promoting approach are marked by filled red circles and are subsequently addressed by ϕ_1 and ϕ_2 . The non-dimensional frequencies of the detected modes, i.e., $Sr_D(\lambda_1) = 0.4$ and $Sr_D(\lambda_2) = 0.63$ closely match the characteristic peaks in the spectra of the pressure fluctuations and temporal coefficients of the first two POD modes.

To investigate the coherent modulation of the flow field described by the two DMD modes, the spatial shape of the modes is considered. Therefore, the respective modes ϕ_1 and ϕ_2 are superimposed with the mean flow given by the mode ϕ_{mean} and reconstructed in time according to Eq. 8. The pressure contours of the resulting flow field are given for the two modes in Fig. 21. Since the shape of the modes is quasi two-dimensional, i.e., they do not alter in the spanwise direction, the pressure is shown in a x-y-plane at $z/D = 0.6$. To illustrate the temporal evolution of the modes, the upper part of the image shows the flow field at the time instance $t = t_0$ while the lower part displays the reconstructed flow at $t = t_0 + 0.5T(\lambda_n)$, where $T(\lambda_n) = D/(Sr_D(\lambda_n) u_\infty)$ is the period duration of the respective mode. The reconstruction of both modes indicates a streamwise harmonic oscillation of the shock pattern which is caused by a change of the shock angle. Therefore, the two modes undergo a coherent motion similar to the POD modes. This confirms the explanation that the detected pressure loads are caused by a shock and shear layer oscillation. In addition, the similarity between the DMD analysis and POD results shows that the most energetic modes are also the dynamical most important modes.

4 Conclusions

The turbulent wake of a planar space launcher equipped with a dual-bell nozzle is numerically investigated to determine the influence of the advanced propulsion concept onto the intricate wake-nozzle flow interaction. The investigation is performed at transonic

freestream conditions, i.e., $M_\infty = 0.8$ and $Re_D = 4.3 \cdot 10^5$, and the dual-bell nozzle is operated at sea-level conditions, i.e., with a flow separation at the contour inflection. A zonal RANS/LES approach combined with a synthetic turbulence generation method is used for the simulations and the results are validated by experimental measurements.

The wake of the BFS is characterized by the shear layer separating at the shoulder of the main body and impinging on the nozzle. The reattachment length strongly varies about the time averaged position. In addition, the recirculation bubble exhibits a strong spanwise variation evidenced by the instantaneous skin-friction distribution, leading to periodic wall pressure fluctuations. The comparison with a conventional TOP nozzle reveals that when the smaller step height and nozzle length are taken into account the overall flow topology downstream of the BFS is hardly affected by the modified nozzle contour. However, the shock and flow separation originating from the nozzle contour inflection and the consequential entrainment of the outer flow into the nozzle cause increased pressure fluctuations at the inner nozzle wall.

Using a temporal Fourier transform of the wall pressure fluctuations on the outer nozzle fairing three distinct peaks at $Sr_D = 0.045$, $Sr_D = 0.14$, and $Sr_D = 0.24$ are detected. The modal analysis of the outer wake flow based on POD and DMD reveals that the dynamic pressure loads are caused by a low frequency growing and contracting separation bubble and a higher frequency oscillating wavy motion of the shear layer. The full three-dimensional reconstruction of the DMD modes exhibits a pronounced three-dimensionality leading to a formation of wave-like structures explaining the wedge-shaped reattachment regions in the skin-friction coefficient distribution. Similar low frequency coherent motions were found in previous investigations with a conventional TOP nozzle and in pure BFS configurations without a jet. Therefore, it is stated that the outer flow downstream of the BFS is not affected by the dual-bell nozzle concept.

To investigate the flow dynamics leading to the increased pressure loads around the jet plume and on the wall of the nozzle extension, temporal Fourier transform of the pressure fluctuations and a POD and DMD analysis of the velocity and pressure field are performed. By the Fourier analysis, three characteristic frequencies at $Sr_D = 0.4$, $Sr_D = 0.61$, and $Sr_D = 0.9$ are extracted. The modal decomposition reveals a periodic streamwise pumping and wave-like motion of the shear layer between the plume and the entrained outer flow within the nozzle extension. The shear layer oscillation is coupled to a streamwise periodic movement of the shock. Overall, this leads to the revealed increased pressure loads at the dual-bell nozzle wall. The results demonstrate that for the present configuration and flow parameter regime, i.e., a planar launcher-like configuration with cold air flow, increased pressure loads act on the inner nozzle wall indicating that particular attention should be paid to the nozzle flow dynamics at sea-level conditions in the design of dual-bell nozzles. However, it still has to be analyzed whether or not similar dynamics and pressure loads occur in more realistic configurations which will be done in future investigations of dual-bell nozzles for axisymmetric space launchers.

Acknowledgements Financial support has been provided by the German Research Foundation (Deutsche Forschungsgemeinschaft – DFG) in the framework of the Sonderforschungsbereich Transregio 40. The authors are grateful for the computing resources provided by the High Performance Computing Center Stuttgart (HLRS) and the Jülich Supercomputing Center (JSC) within a Large-Scale Project of the Gauss Center for Supercomputing (GCS)

Funding This study was funded by the German Research Foundation (DFG).

Compliance with Ethical Standards

Conflict of interests The authors declare that they have no conflict of interest.

References

1. Stark, R., Génin, C.: Sea-level transitioning dual bell nozzles. *CEAS Space J.* **9**, 279–287 (2017)
2. Proshchanka, D., Koichi, Y., Tsukuda, H., Araki, K., Tsujimoto, Y., Kimura, T., Yokota, K.: Jet oscillation at low-altitude operation mode in dual-bell nozzle jet oscillation at low-altitude operation mode in dual-bell nozzle jet oscillation at low-altitude operation mode in dual-bell nozzle. *J. Propuls. Power* **28**(5), 1071–1080 (2012)
3. Martelli, E., Nasuti, F., Onofri, M.: Numerical parametric analysis of dual-bell nozzle flows. *AIAA J.* **45**(3) (2007)
4. Schneider, D., Génin, C.: Numerical investigation of flow transition behavior in cold flow dual-bell rocket nozzles. *J. Propuls. Power* **32**(5), 1212–1219 (2016)
5. Bradshaw, P., Wong, F.: The reattachment and relaxation of a turbulent shear layer. *J. Fluid Mech.* **52**(1), 113–135 (1972)
6. Eaton, J.K., Johnston, J.P.: A review of research on subsonic turbulent flow reattachment. *AIAA J.* **19**(9), 1093–1100 (1981)
7. Driver, D.M., Seegmiller, H.L., Marvin, J.G.: Time-dependent behavior of a reattaching shear layer. *AIAA J.* **25**(7), 914–919 (1987)
8. Friedrich, R., Arnal, M.: Analysing turbulent backward-facing step flow with the low-pass-filtered Navier-Stokes equations. *J. Wind Eng. Ind. Aerodyn.* **35**, 101–128 (1990)
9. Silveria Neto, A., Grand, D., Metais, O., Lesieur, M.: A numerical investigation of the coherent vortices in turbulence behind a backward-facing step. *J. Fluid Mech.* **256**, 1–25 (1993)
10. Le, H., Moin, P., Kim, J.: Direct numerical simulation of turbulent flow over a backward-facing step. *J. Fluid Mech.* **330**, 349–374 (1997)
11. Lee, I., Sung, H.J.: Characteristics of wall pressure fluctuations in separated and reattaching flows over a backward-facing step: Part I. Time-mean statistics and cross-spectral analyses. *Exp. Fluids* **30**, 262–272 (2001)
12. Statnikov, V., Bolgar, I., Scharnowski, S., Meinke, M., Kähler, C.J., Schröder, W.: Analysis of characteristic wake flow modes on a generic transonic backward-facing step configuration. *Europ. J. Mech. B/Fluids* **59**, 124–134 (2016)
13. Scharnowski, S., Bolgar, I., Kähler, C.J.: Characterization of turbulent structures in a transonic backward-facing step flow. *Flow, Turbul. Combust.*, 1–21 (2016)
14. Bolgar, I., Scharnowski, S., Kähler, C.J.: The effect of the mach number on a turbulent backward-facing step flow. *Flow Turbul. Combust.* **101**(3), 653–680 (2018)
15. Deprés, D., Reijasse, P., Dussauge, J.P.: Analysis of unsteadiness in afterbody transonic flows. *AIAA J.* **42**(12), 2541–2550 (2004)
16. Deck, S., Thorigny, P.: Unsteadiness of an axisymmetric separating-reattaching flow: Numerical investigation. *Phys. Fluids*, **19**(065103) (2007)
17. Schrijer, F., Sciacchitano, A., Scarano, F.: Spatio-temporal and modal analysis of unsteady fluctuations in a high-subsonic base flow. *Phys. Fluids*, **26**(086101) (2014)
18. Statnikov, V., Meinke, M., Schröder, W.: Analysis of spatio-temporal wake modes of space launchers at transonic flow. *AIAA Paper*, 2016–1116 (2016)
19. Statnikov, V., Meinke, M., Schröder, W.: Reduced-order analysis of buffet flow of space launchers. *J. Fluid Mech.* **815**, 1–25 (2017)
20. Bolgar, I., Scharnowski, S., Kähler, C.J.: Experimental analysis of the interaction between a dual-bell nozzle with an external flow field aft of a backward-facing step. 21 DGLR-Fach-Symposium der STAB (2018)
21. Loosen, S., Statnikov, V., Meinke, M., Schröder, W.: Numerical investigation of the turbulent wake of a generic space launcher at transonic speed. In: 7th European Conference for Aeronautics and Aerospace Sciences, <https://doi.org/10.13009/EUCASS2017-561> (2017)
22. David, S., Radulovic, S.: Prediction of buffet loads on the Ariane 5 afterbody. In: 6th International Symposium on Launcher Technologies. Munich, Germany 8–11 November (2005)
23. Fares, E., Schröder, W.: A general one-equation turbulence model for free shear and wall-bounded flows. *Flow Turbul. Combust.* **73**, 187–215 (2004)

24. Statnikov, V., Sayadi, T., Meinke, M., Schmid, P., Schröder, W.: Analysis of pressure perturbation sources on a generic space launcher after-body in supersonic flow using zonal turbulence modeling and dynamic mode decomposition. *Phys. Fluids*, **27**(016103) (2015)
25. Roidl, B., Meinke, M., Schröder, W.: A reformulated synthetic turbulence generation method for a zonal RANS-LES method and its application to zero-pressure gradient boundary layers. *Int. J. Heat Fluid Flow* **44**, 28–40 (2013)
26. Roidl, B., Meinke, M., Schröder, W.: Boundary layers affected by different pressure gradients investigated computationally by a zonal RANS-LES method. *Int. J. Heat Fluid Flow* **45**, 1–13 (2014)
27. Jarrin, N., Benhamadouche, S., Laurence, D., Prosser, R.: A synthetic-eddy-method for generating inflow conditions for large-eddy simulations. *Int. J. Heat Fluid Flow* **27**, 585–593 (2006)
28. Choi, H., Moin, P.: Grid-point requirements for large eddy simulation: Champan's estimates revisited. *Phys. Fluids*, **24**(011702) (2012)
29. Berkooz, G., Holmes, P., Lumley, J.L.: The proper orthogonal decomposition in the analysis of turbulent flows. *Annu. Rev. Fluid Mech.* **25**(1), 539–575 (1993)
30. Taira, K., Brunton, S.L., Dawson, S.T.M., Rowley, C.W., Colonius, T., McKeon, B.J., Schmidt, O.T., Gordeyev, S., Theofilis, V., Ukeiley, L.S.: Modal analysis of fluid flows: An overview. *AIAA J* (2017)
31. Schmid, P.J.: Dynamic mode decomposition of numerical and experimental data. *J. Fluid Mech.* **656**, 5–28 (2010)
32. Jovanovic, M.R., Schmid, P.J., Nichols, J.W.: Sparsity-promoting dynamic mode decomposition. *Phys. Fluids*, **26**(024103) (2014)
33. Winant, C.D., Browand, F.K.: Vortex pairing: The mechanism of turbulent mixing-layer growth at moderate Reynolds number. *J. Fluid Mech.* **63**(2), 237–255 (1974)

Publisher's Note Springer Nature remains neutral with regard to jurisdictional claims in published maps and institutional affiliations.